Optics Letters

Wavelength-dependent optical detection of strain waves near intrinsic and artificial optical resonances

Thomas J. van den Hooven[1,*] **and Paul C. M. Planken**[1,2]

[1]Advanced Research Center for Nanolithography, Science Park 106, Amsterdam 1095 XG, The Netherlands
[2]Van der Waals-Zeeman Institute, Institute of Physics, University of Amsterdam, Science Park 904, Amsterdam 1098 XH, The Netherlands
*t.vdhooven@arcnl.nl

Received 5 December 2024; revised 12 January 2025; accepted 22 January 2025; posted 23 January 2025; published 18 February 2025

Laser-induced, ultrafast strain waves are potentially interesting for subsurface metrology in the semiconductor industry. These waves are commonly detected by measuring their effect on the reflectance of a material. Changes in reflectance are typically small, making detection difficult. In this Letter, we compare strain-wave-induced changes in reflectance at and around an interband transition (IBT) and a surface plasmon polariton resonance (SPR). Both are present on an Au-covered segmented grating, at different wavelengths. Using a white light continuum (WLC) probe pulse, we measure ultrafast reflectance changes over a broad wavelength range. We find that the strain-wave-induced changes at the IBT are only about 37% smaller than those measured with probe wavelengths close to an SPR. This contrasts with the different appearance of the SPR and the IBT in the static reflectance spectrum of the sample. Our results show that the static reflectance spectrum is not a good predictor for the strain-wave-induced reflectance changes and emphasize the importance of experiments to find the optimum wavelength to detect strain waves.

© 2025 Optica Publishing Group under the terms of the Optica Open Access Publishing Agreement

https://doi.org/10.1364/OL.551109

Ultrafast strain waves, generated and detected with ultrashort optical pulses [1,2], can penetrate optically opaque layers to measure layer thickness [3] and detect subsurface structures [4,5]. This hybrid optical and acoustic technology is a promising candidate for subsurface metrology in the semiconductor manufacturing industry, e.g., for wafer alignment [6,7]. Unfortunately, achieving the signal-to-noise ratio (SNR) required for the detection of strain waves in these applications is challenging. Strain waves can dynamically alter the complex refractive index of a material and, thus, its reflectance, which can be measured using an ultrashort laser pulse. However, the magnitude of these changes may be small or even non-existent for specific probe wavelength and acoustic frequency combinations [8].

Interestingly, strain-wave-induced reflectance changes can non-trivially depend on the probe wavelength, which may provide an easy path toward increasing signal strength. Probing with wavelengths close to the IBT in aluminum, e.g., has shown to dramatically modify the strain-wave-induced reflectance changes [9]. A similar, strong wavelength dependence in the detection of strain waves has also been observed when probing close to SPRs. Surface plasmon polariton are collective oscillations of free electrons in a metal, coupled to an electromagnetic wave. They can be used to enhance the detection of strain waves on, e.g., flat surfaces [10,11] or metallic gratings [12]. Although the latter require surface modifications, they have an advantage over the intrinsic IBT: They can be tailored to be resonant for a specific (optical) wavelength range.

For metrology applications, however, a quantitative analysis of the enhancements due to the naturally occurring IBTs and the "artificial" SPRs is essential. This is challenging, as it should ideally be conducted using a single sample under the same experimental conditions. Such a comparison is also interesting because the two resonances manifest themselves differently in the linear reflectance spectrum of gold. The IBT shows up as a gradually decreasing reflectance when the wavelength decreases from 600 nm to 475 nm, while the SPR has a sharp dip in the reflectance.

In this Letter, we show the strain-wave-induced changes in reflectance of an Au-covered segmented grating, for probe wavelengths between 465 nm and 755 nm. This wavelength range simultaneously covers the IBT of Au at approximately 520 nm (2.4 eV, [13]) and three SPRs at 615 nm, 652 nm, and 695 nm [14] (2.0 eV, 1.9 eV, and 1.78 eV, respectively).

We observe time-dependent oscillatory changes in reflectance near both the IBT and near the SPRs, which correspond to a 9.5 GHz longitudinal wave (LW) excited by the pump pulse. The largest change in the reflectance is measured on the *slope* of the SPR, at a wavelength of 649 nm. Near the IBT, the amplitude of the reflectance has a maximum at a probe wavelength of 510 nm (2.43 eV), and the amplitude is about 37 % smaller than that measured close to the SPR. This difference in the strain-wave-induced reflectance changes measured around the SPR and IBT contrasts with the large difference in shape of the static reflectance spectrum around these optical resonances. It shows that for resonances that have different physical origins, the static reflectance spectrum is not a good predictor of the relative strength of the optical changes induced by the strain waves. It thus highlights the need to perform wavelength-dependent measurements to maximize the strain-wave-induced reflectance changes.

The sample is a segmented grating, similar to what is sometimes used in the semiconductor industry for wafer alignment.

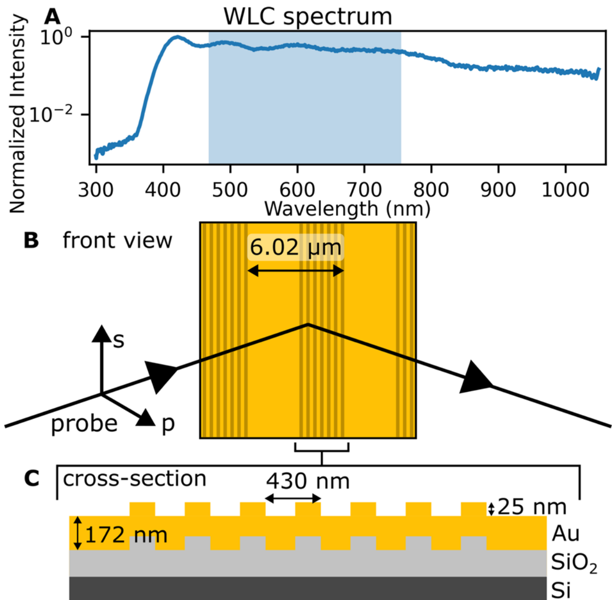

Fig. 1. (A) Visible part of the WLC spectrum; the shaded area indicates the wavelength range used in the experiments. (B) Front view of the segmented grating, on which the probe light is incident. (C) Schematic cross section of the sample.

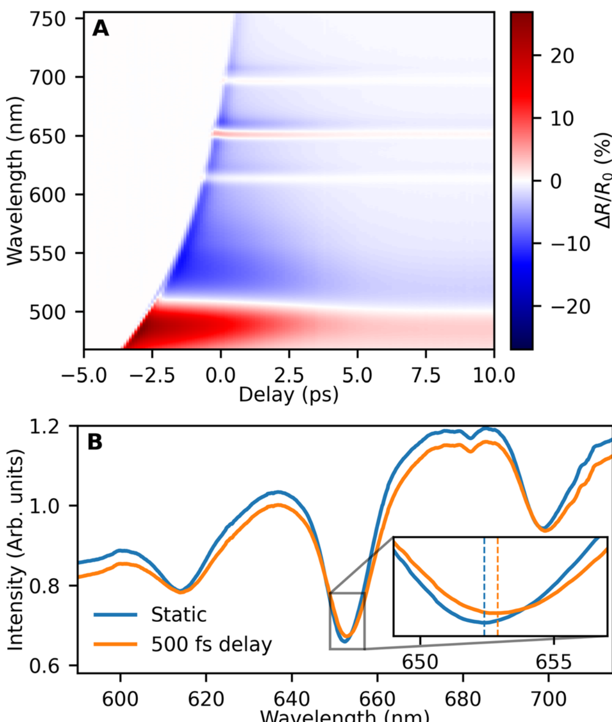

Fig. 2. (A) Relative change in reflectance as a function of pump–probe time delay and probe wavelength. (B) Part of the static and pumped (delay 500 fs) reflectance spectrum, normalized by the reference spectrum. The inset highlights the change in shape and central wavelength of the SPR.

The grating is covered by 172 nm of Au and is shown schematically in Figs. 1(B) and 1(C). The segmented grating is a short-period grating (Λ_{SPP} = 430 nm), capable of sustaining surface plasmon polaritons (SPPs) in the visible, amplitude modulated with a long-period grating (Λ = 6020 nm). Due to the amplitude modulation, the grating also contains "sideband gratings" at the sum and difference spatial frequencies of the two gratings [14]. At these sidebands, SPPs can also be excited, giving a total of *three* SPRs, at 615 nm, 652 nm, and 695 nm, in line with earlier experiments, for *p*-polarized light with an angle of incidence (AOI) of 26° with respect to the surface normal. The SPRs can be seen as dips in the reflectance of the sample as shown in Fig. 6(B).

In the experiments, 400 nm pulses, with a peak fluence of about 6.2 mJ cm^{-2}, generate strain waves in the sample. The pump polarization is parallel to the grating lines and cannot excite SPPs on the sample.

The 1200 nm output of an optical parametric amplifier (OPA) is focused into a 2 mm thick barium fluoride (BaF_2) crystal to generate a WLC probe pulse. Figure 1(A) shows a part of the spectrum of a typical WLC pulse. A broadband beam splitter, reflecting about 70 %, splits the WLC into two, where the transmitted part is measured as a reference spectrum. The reflected part is focused onto the sample, such that the probe spot diameter is about 6.5 times smaller than the pump. The probe AOI is about 26° with respect to the surface normal, in the plane perpendicular to the grating lines, as shown schematically in Fig. 1(B). The reflection from the sample is collimated and measured by the spectrometer. Any probe light *diffracted* from the sample is blocked. The spectrometer is built around a high-speed CMOS camera (Andor Zyla 4.2 PLUS, Oxford Instruments). More information can be found in Supplement 1.

In Fig. 2(A), we plot the pump-induced relative changes in reflectance as a function of probe wavelength, for pump–probe delays between −5 ps and +10 ps. In this time window, the large and rapid changes in reflectance, followed by a slower decay, are caused by electron gas heating and cooling [15]. We note that a clear positive chirp is visible, as there is a wavelength-dependent shift in time of the abrupt reflectance change toward more negative delays, for decreasing the probe wavelength.

Despite the chirp, the individual wavelength components are still able to probe a rapid (rise time <300 fs) change in reflectance when the pump pulse arrives. For the shortest wavelengths, up to 510 nm, the reflectance rapidly increases by up to 25 % and then decays almost linearly to an increase of about 2.5 % at 10 ps. For wavelengths between 510 nm and 600 nm, the reflectance initially *decreases* by up to 15 %, before recovering to a decrease of about 1 %, which is consistent with earlier results [16,17]. The zero-crossing between the positive and negative changes in reflectance shifts from 510 nm to 500 nm in this time interval. The change in sign of the reflectance change as a function of wavelength around the IBT is caused by *Fermi smearing* [16–20].

For wavelengths longer than 600 nm, the initial change in reflectance is still negative, but its amplitude decreases with increasing wavelength: The effects of Fermi smearing decrease as the photon energies become (much) smaller than the IBT threshold energy [17]. Furthermore, the initial reflectance change appears to recover faster for longer wavelengths.

The heating of the electron gas also affects the three SPRs: Fig. 2(B) shows both the static reflectance spectrum and the reflectance spectrum 500 fs after the pump pulse for wavelengths between 590 nm and 715 nm. The absorption dips in the reflectance spectrum become a bit more shallow, and their central wavelengths shift to slightly longer wavelengths, as is

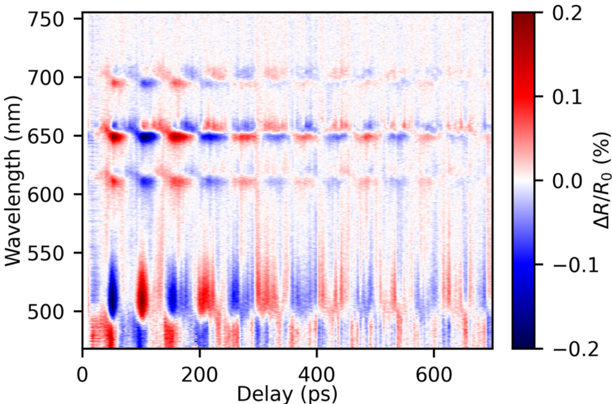

Fig. 3. High-pass filtered reflectance changes for *p*-polarized probe light as a function of pump–probe time delay and probe wavelength. A 5 × 5 smoothing filter has been applied.

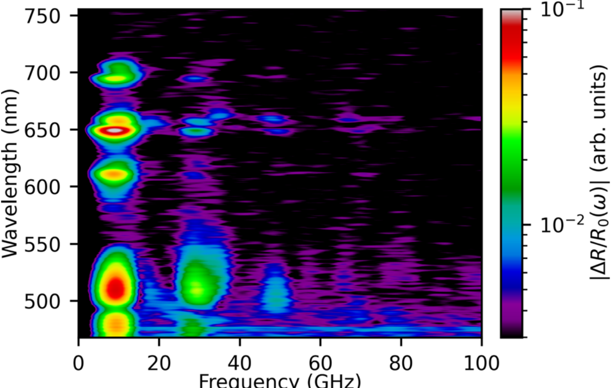

Fig. 5. Amplitude of the reflectance changes in the first 300 ps as a function of strain-wave frequency and probe wavelength. A 5 × 5 smoothing filter has been applied.

shown in the inset. The change in shape is commonly attributed to a change in the imaginary part of the dielectric function of the metal, whereas the shift is attributed to a change in the real part [21–23]. After a few ps, the changes have mostly decayed, the residual change in reflectance is due to the lattice heating.

The remaining energy in the lattice dissipates into the substrate over several nanoseconds, resulting in a slowly decreasing reflectance change, present at all wavelengths. This thermal background masks the fast strain-wave-induced reflectance changes. To show these, we filter the reflectance changes using an eighth-order high-pass zero-phase digital Butterworth filter, with a cut-off frequency of 6 GHz. This also removes the low-frequency surface acoustic wave (SAW) [14] as we focus only on the LWs.

Figure 3 shows the filtered reflectance changes as a function of probe wavelength and pump–probe delay time, on a time scale of 700 ps. Strain-wave-induced oscillations in the reflectance, with a period of 105 ps, are visible for probe wavelengths shorter than 550 nm and near the three SPRs, at 615 nm, 650 nm, and 695 nm. The oscillation period of 105 ps matches the round trip time of the longitudinal acoustic wave in the 172 nm thick Au layer [14]. Around all three SPRs, the phase of the oscillation changes abruptly when the wavelength changes from below to above each resonance. Interestingly, a similar phase jump is present near the IBT, at about 500 nm.

In Fig. 4, we plot the reflectance changes as a function of delay time for probe wavelengths of 480 nm, 520 nm, 648 nm,

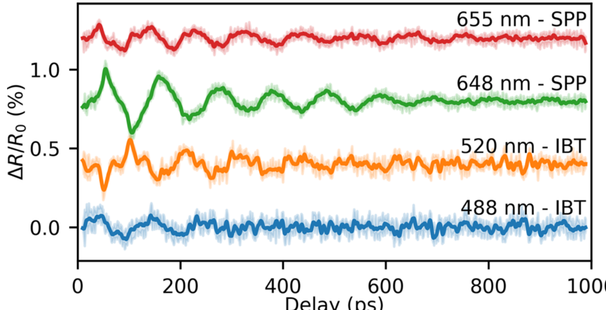

Fig. 4. High-pass filtered reflectance changes of selected wavelengths; the shaded area indicates the minimum and maximum values of the five wavelengths closest to the indicated wavelength. The curves are offset for visibility.

and 655 nm. Each curve is the average of five wavelengths closest to, and including, the indicated wavelength, and the maximum and minimum values within those pixels are shown by the shaded areas. The figure highlights that the oscillations of the reflectance changes measured on either side of the resonance or transition have an almost opposite phase.

For small delays (<250 ps), the reflectance change at 648 nm is a more or less triangularly shaped wave, indicating that it consists of the fundamental longitudinal mode and odd higher modes [24]. Only the odd modes are excited because the thermal stress in the layer is nearly constant as a function of depth [25]. The latter is caused by the rapid transfer of absorbed energy from close to the surface, deeper into the layer due to ballistic electron transport and electron energy diffusion [16]. Interestingly, the reflectance change measured at 520 nm, with photon energies just below the IBT threshold energy, has a different temporal shape.

Figure 5 shows the fast Fourier transform (FFT) of the first 300 ps of the reflectance changes of all measured wavelengths, for *p*-polarized light. A Hann window is used to reduce windowing artifacts. We measure the highest amplitude for the fundamental LW frequency of 9.5 GHz at 649 nm, on the short-wavelength side of the strongest SPR at 650 nm. The strain-wave-induced reflectance changes at the other two SPRs also show a larger amplitude on the short-wavelength side.

Naively, we would expect a π phase shift when comparing the probe wavelengths below and above the SPRs. Instead, we measure a 0.7π phase shift, for each of the three resonances. The most likely explanation for this is that the strain wave changes the complex dielectric function by some complex value $\delta\epsilon$. The real part of $\delta\epsilon$ affects the central wavelength of the SPR. A shifting central wavelength can result in opposite reflectance changes on either side of the SPRs. This would imply that the phase changes by exactly π over the SPR. However, the *imaginary* part of $\delta\epsilon$ results in a change in reflectance that is symmetric around the central wavelength of the SPR [10]. The combined contribution of $\delta\epsilon$ can result in an apparent total change less than π.

Near the IBT, the fundamental mode reaches its highest amplitude at 510 nm (2.43 eV), corresponding to a photon energy approximately equal to the IBT threshold energy of 2.4 eV. Interestingly, the strain-wave-induced changes are about 37% smaller for wavelengths at and close to the IBT than for those near the largest SPR (at 649 nm). This is in remarkable contrast

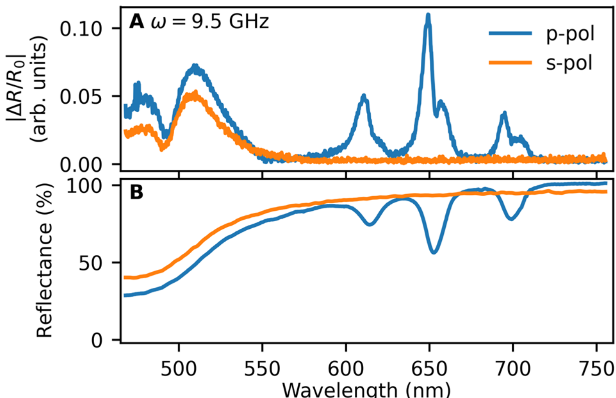

Fig. 6. (A) Amplitude of reflectance changes induced by the 9.5 GHz strain wave, for *p*- and *s*-polarized probe light. A moving average has been applied using two neighboring values. (B) Static reflectance, for *p*- and *s*-polarized light, as a function of wavelength, for an AOI of 26°; see also Supplement 1.

with the reflectance changes induced by the *electron dynamics* immediately following the pump pulse illumination. There, the reflectance changes near the IBT are significantly larger than those near any of the SPRs.

The third- and fifth-order harmonic modes, at frequencies of 28.5 GHz and 47 GHz, respectively, have the largest amplitude reflectance changes at 510 nm. The amplitude at this probe wavelength, relative to the first-order mode, is much higher than near any of the SPRs.

For *s*- and *p*-polarized probe light, we plot in Fig. 6(A) the FFT amplitude of the reflectance changes at 9.5 GHz as a function of probe wavelength. The changes in reflectance for *s*-polarized light in the time domain are shown in Supplement 1. As mentioned before, significant reflection changes occur near the SPRs for *p*-polarized light and are, as expected, absent for *s*-polarized light. Around the IBT, strain-wave-induced reflectance changes are present for both polarizations.

In Fig. 6(B), we plot the static reflectance of the sample for *p*- and *s*-polarized light. The SPRs, visible as dips in the *p*-polarized reflectance spectrum, coincide with the regions of enhanced strain-wave-induced reflectance changes. Upon careful inspection, these changes peak at wavelengths that are actually on the slope of the dips. However, near the IBT, such sharp features are absent in the static reflectance spectra, yet large strain-wave-induced changes are measured there.

The results show that the shape of the static linear reflectance spectrum around SPRs and IBT is not a good predictor of the amplitude of the strain-wave-induced reflectance changes. Whereas the SPRs are sharp and the IBT manifests itself as a more gradual change in reflectance, the strain-wave-induced reflectance changes are only about 37 % smaller near the IBT, compared to the amplitude near the SPRs. However, the temporal shape of the reflectance changes is significantly different when probing around the IBT compared to the SPRs. In the absence of a model that can accurately predict these signals, the conclusion is that wavelength-dependent measurements are required to determine the maximum strain-wave-induced reflectance changes when resonances of a different nature are present.

Acknowledgment. This work was conducted at the Advanced Research Center for Nanolithography, a public–private partnership between the University of Amsterdam, Vrije Universiteit Amsterdam, University of Groningen, the Netherlands Organization for Scientific Research (NWO), and the semiconductor equipment manufacturer ASML.

Disclosures. The authors declare no conflicts of interest.

Data availability. Data underlying the results presented in this Letter are not publicly available at this time but may be obtained from the authors upon reasonable request.

Supplemental document. See Supplement 1 for supporting content.

REFERENCES

1. C. Thomsen, H. T. Grahn, H. J. Maris, *et al.*, Phys. Rev. B **34**, 4129 (1986).
2. P. Ruello and V. E. Gusev, Ultrasonics **56**, 21 (2015).
3. O. Wright, T. Hyoguchi, and K. Kawashima, Nondestr. Test. Eval. **7**, 149 (1992).
4. B. C. Daly, N. C. R. Holme, T. Buma, *et al.*, Appl. Phys. Lett. **84**, 5180 (2004).
5. A. Antoncecchi, H. Zhang, S. Edward, *et al.*, Opt. Express **28**, 33937 (2020).
6. S. Edward, H. Zhang, I. Setija, *et al.*, Phys. Rev. Appl. **14**, 014015 (2020).
7. A. J. den Boef, Surf. Topogr.: Metrol. Prop. **4**, 023001 (2016).
8. C. He, O. Ristow, M. Grossmann, *et al.*, Phys. Rev. B **95**, 184302 (2017).
9. A. Devos and A. Le Louarn, Phys. Rev. B **68**, 045405 (2003).
10. F. Noll, N. Krauß, V. Gusev, *et al.*, Photoacoustics **30**, 100464 (2023).
11. M. van Exter and A. Lagendijk, Phys. Rev. Lett. **60**, 49 (1988).
12. G. de Haan, V. Verrina, A. J. L. Adam, *et al.*, Appl. Opt. **60**, 7304 (2021).
13. N. E. Christensen and B. O. Seraphin, Phys. Rev. B **4**, 3321 (1971).
14. T. J. van den Hooven and P. C. M. Planken, Photoacoustics **31**, 100497 (2023).
15. S. Anisimov, B. Kapeliovich, and T. Perel'man, Zh. Eksp. Teor. Fiz. **66**, 776 (1974).
16. J. Hohlfeld, S.-S. Wellershoff, J. Güdde, *et al.*, Chem. Phys. **251**, 237 (2000).
17. R. W. Schoenlein, W. Z. Lin, J. G. Fujimoto, *et al.*, Phys. Rev. Lett. **58**, 1680 (1987).
18. V. V. Kruglyak, R. J. Hicken, P. Matousek, *et al.*, Phys. Rev. B **75**, 035410 (2007).
19. C.-K. Sun, F. Vallée, L. H. Acioli, *et al.*, Phys. Rev. B **50**, 15337 (1994).
20. R. Hayashi, A. Iwasaki, P. Vasa, *et al.*, AIP Adv. **12**, 095207 (2022).
21. A. Devizis, V. Vaicikauskas, and V. Gulbinas, Appl. Opt. **45**, 2535 (2006).
22. A. A. Kolomenskii, R. Mueller, J. Wood, *et al.*, Appl. Opt. **52**, 7352 (2013).
23. R. Groeneveld, R. Sprik, and A. Lagendijk, Phys. Rev. Lett. **64**, 784 (1990).
24. M. Schubert, M. Grossmann, C. He, *et al.*, Ultrasonics **56**, 109 (2015).
25. F. Hudert, A. Bruchhausen, D. Issenmann, *et al.*, Phys. Rev. B **79**, 201307 (2009).